Supporting Information

for

Chain-Length-Selective Adsorption Governs Diffusion-Limited Dendrite Growth Mode in Battery Electrodes

Aakriti Aggarwal[1], Wenrui Chai[2], Graeme Henkelman[2], Kent J.X. Zheng[1,3,4]*

1. Department of Chemical Engineering, University of Texas at Austin, Austin, Texas 78712, USA

2. Department of Chemistry, University of Texas, Austin, Texas 78712, USA

3. Texas Materials Institute, University of Texas at Austin, Austin, Texas 78712, USA

4. Bard Center for Electrochemistry, University of Texas at Austin, Austin, Texas 78712, USA

Materials and Methods

Electrochemical measurements

The experiment was conducted using a cuvette open cell with a 3-electrode symmetric cell setup. The working, reference and counter electrodes were all Zn foil purchased from MSE supplies (99.9%, 0.1mm thickness). The basic electrolyte chosen was 10 M ZnCl2 in an aqueous solution (chosen as a viable Zn metal anode battery electrolyte), prepared within vials under ambient air using ZnCl2 (98-100.5%, puriss. grade) and deionized water.[1, 2] Chosen amounts of selected polymers were added by weight percent to a large batch of prepared 10M ZnCl2 electrolyte. The electrochemical measurements were conducted using a CHI 1100D electrochemical station (CH instrument, USA) for constant potential conditions and an SP-200 potentiostat (Biologic, France) for constant current conditions. For each cell tested. Synchronous in-operando visualization was conducted using a high-resolution digital microscope (UMH210-11, AmScope). The constant potential experiments were run at $V_{over\text{-}limiting}$ to ensure diffusion limited dendritic growth (refer to previous work for the full definition).[3] The constant current measurements were run similarly at $J_{over\text{-}limiting}$ current density.[3] These conditions were kept constant for all experiments conducted. $V_{over\text{-}limiting}$ and $J_{over\text{-}limiting}$ at approximately 3 times the limiting current and hence promote dendritic growth in the electrochemical cell set-up used in this work.

Electrochemical Impedance Spectroscopy Measurements

PEIS measurements were conducted using an SP-200 potentiostat (Biologic, France) at OCP, i.e. 0.0V against reference. Since the measurements were taken using a 2-electrode set-up, the reference lead was connected to the counter electrode. The scan was performed over a frequency range of 1 MHz to 100 mHz with 6 points per decade and single sinusoidal excitation signal with

an amplitude of 5.0 mV. The measurements were initially made every 30s immediately after running the constant current electro-deposition protocol, but the increments were increased to 3 minutes for the IN growth since the progression of the dendritic front was about 3 times slower in comparison to CG growth.

NMR Measurements

First, 10M ZnCl2 was prepared under ambient air using the same salt with deuterated water in vials. Then for each polymer chain length, one solution was prepared by adding 1 wt% of the same polymer from the electrochemical measurements to the prepared 10M ZnCl2 solution; another was made by adding 1wt% of the polymer to just deuterated water. Then, the ^{1}H-NMR spectra were collected on an Agilent MR400 spectrometer. Each of the spectra were referenced to D2O solvent peaks (D2O = 4.78 ppm) in order to cross-analyze.

QCM-D Measurements

The electrolytes were prepared as described for the electrochemical measurements. The measurements were conducted using Q-Sense E-1 system (Biolin Scientific) using the Q-sense Flow Module for 5 MHz Sensors. The sensor used was Gold, Ti adhesion layer Q sensor (nanoScience Instruments), cleaned using de-ionized water rinse followed by UV-ozone treatment for 10 minutes between runs. A peristaltic pump was used at a flow rate of 300 uL/min to flow de-ionized water for 5 minutes, followed by 10M ZnCl2 for 5 minutes, then chosn electrolyte for 5 minutes, followed by 10M ZnCl2 and de-ionized water for 5 minutes each respectively. This process was repeated for each electrolyte system at least 3 times to ensure repeatability.

FTIR Measurements

A Bruker Invernio R FTIR machine was used with an Attenuated Total Reflectance (ATR) module to measure transmittance spectra. The solutions were drop-casted onto the crystal, with a blank measurement of ambient air. The solutions chosen were 80 wt% polymer with 20 wt% deionized water, with and without 10M ZnCl2 in the 80/20 solution. This was chosen for two reasons: (1) the normal 1 wt% electrolyte spectrum would be fully dominated by water instead of relevant interaction between polymer and salts, (2) at least 20 wt% water is required in order to fully solvate the ZnCl2 salt. The spectra were then analyzed using fityk curve fitting software.

Raman Measurements

A Witec Micro-Raman Spectrometer Alpha 300 machine fitted with a 532 nm laser and a 20x objective was used to collect the spectra. An acquisition time of 1s accumulated over 50 spectra was chosen. First, a grating of 600 was used with a spectral center of 2150, followed by an 1800 grating with spectral center of 3400 or 3500 was used to observe closer the O-H vibrational peak. The electrolytes were prepared similarly to the electrochemical measurements electrolyte using deuterated water.

Viscosity Measurements

An SV-100 Viscometer was used to measure the viscosity of chosen electrolytes. 10 mL of each sample was used for the measurements, conducted at room temperature.

DFT Calculation

Density functional theory (DFT) calculations done with the Vienna Ab-Initio Package.[4-7] Core electrons are described within the projected augmented wave framework; valence electrons are described with a plane wave basis set up to an energy cutoff of 300 eV.[8] The generalized gradient approximation in the form of the Perdew, Burke and Ernzehof functional is used to

model electronic exchange and correlation.[9] Van der Waals interactions are calculated using the DFT-D2 method.[10] The Zn bulk is optimized using a unitcell and the Brillouin zone integration is done using a $17 \times 17 \times 17$ Monkorst k-points mesh.[11] For all surface calculations, the Brillouin zone integration is done at the gamma point only. A 16 Å vacuum layer was used between periodic slab images. After adsorption of the Zn adatom and PEG molecule, this leaves approximately 10 Å of vacuum separation, sufficient to avoid spurious interactions between periodic images.

Some of the low Miller index surfaces were studied, including the $(002), (100), (101), (102), (103)$, and $(21\bar{3})$ surfaces. For all surfaces, the unit cell is repeated enough times to generate at least four layers of Zn atoms so that the bottom two layers of atoms can be constrained to their bulk positions.

Surface calculations in the vacuum is calculated using Equation 1:

$$E_{surf} = \frac{E_{slab} - n\, E_{Zn}}{2\, A_{slab}} \qquad \text{Equation (1)}$$

Where E_{surf} is the surface energy, E_{slab} is the energy of the slab model, n is the number of Zn atoms in the slab model, E_{Zn} is the energy of a Zn atom in bulk, and A_{slab} is the surface area of the slab. The surface energies in the presence of water or $PEG_{n=x}$ where $x = 1,2,4,5$ are approximated when the slab is bond with 4 H_2O molecules, 4 ethylene glycol molecules, or 1 $PEG_{n=2,4,5}$ molecule, respectively. These surface energies are calculated using Equation 2 where $E_{sol-surf}$ is the surface energy with solvent present, $E_{slab+sol*}$ is the energy of the slab model with m surface adsorbed solvent molecules, E_{sol} is the energy of the solvent molecules in vacuum. This crude approach great overestimates the stabilization of surfaces from the presence of solvent molecules as the references for the solvent molecules are in gas phase rather than

solvated liquid or aqueous phase molecules. However, the focus here is not accurately determining the solvated surface energy, but to show the qualitative changes and trends when different solvent or solute molecules are present at the surface.

$$E_{sol-surf} = \frac{E_{slab+sol*} - n\,E_{Zn} - mE_{sol}}{2\,A_{slab}} \qquad \text{Equation (2)}$$

The adatom binding energy is calculated using Equation 3 where $E_{ad-bind}$ is the binding energy of the adatom, $E_{slab+Zn*}$ is the energy of a slab with an adatom that's stabilized by solvent molecules on the surface.

$$E_{ad-bind} = E_{slab+Zn*} - (n+1)E_{Zn} - m\,E_{sol} \qquad \text{Equation (3)}$$

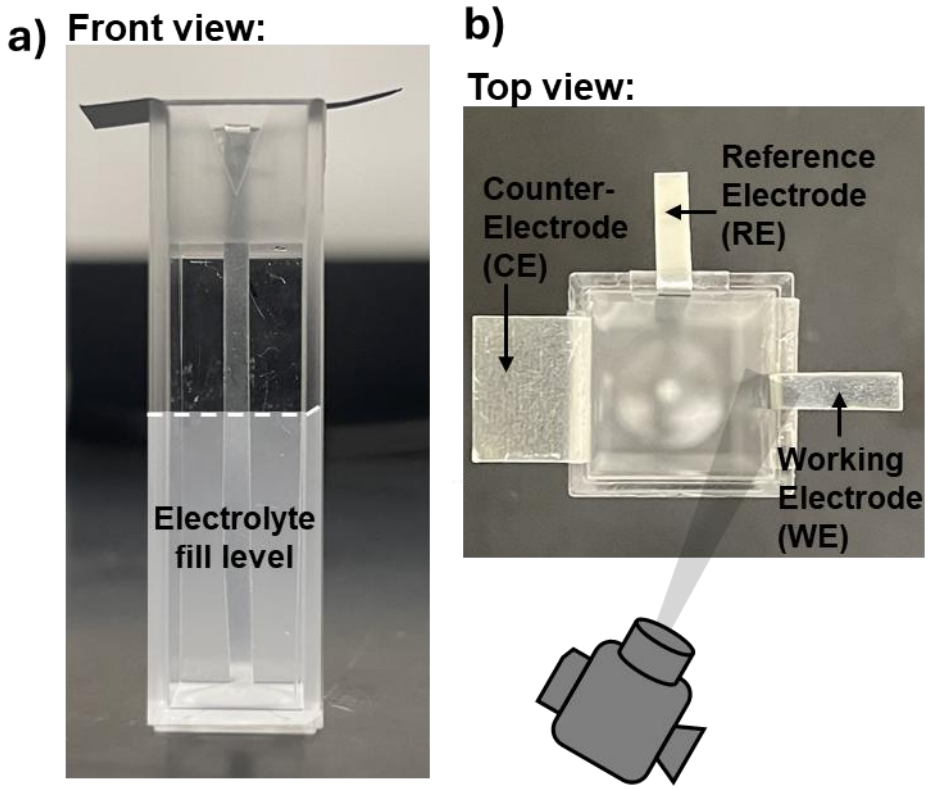

Figure S1: Making the Operando visualization measurements. The cell set-up shown above was used to make all measurements, with the camera seeing the 'front view' shown in panel (a) and the potentiostat connected to the appropriate leads indicated by panel (b). The camera was angled in such a way as to see the surface of the working electrode either flat or at a 30° angle and shown in panel (b). The presence of natural convection (gravity pointing downwards) was a constant unchanged background condition in all experiments conducted and consequently could not serve as a mechanism for the relative change in growth mode.

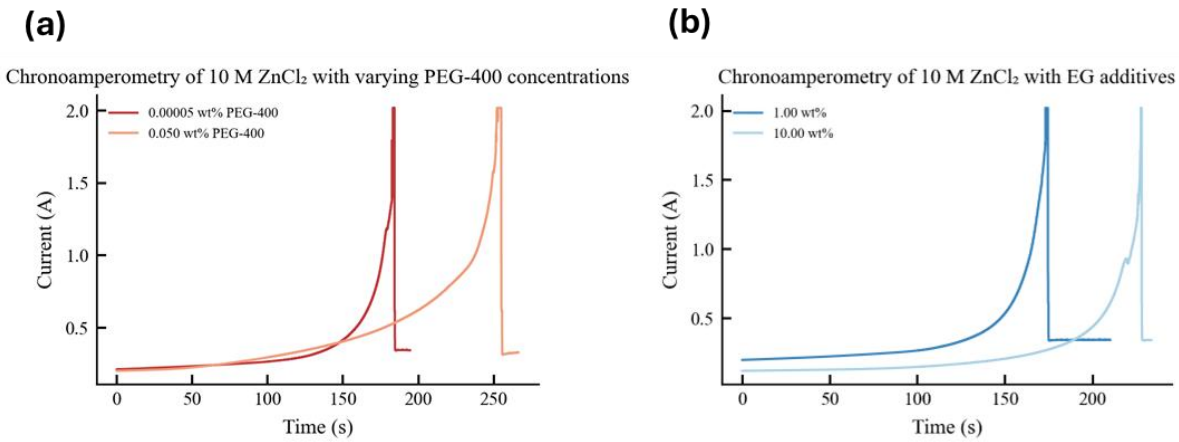

Figure S2: **Representative current transients from the standard electrodeposition protocol.** The sharp fall after the peaks shows shorting behavior**. (a)** Two representative concentrations of PEG-400 additive current transient from chronoamperometry as described in the methods section. 0.05 wt% showed Mode II growth and 0.00005wt% showed Mode I growth. **(b)** Two representative concentrations of EG additive current transients from chronoamperometry. Only Mode 1 growth was seen.

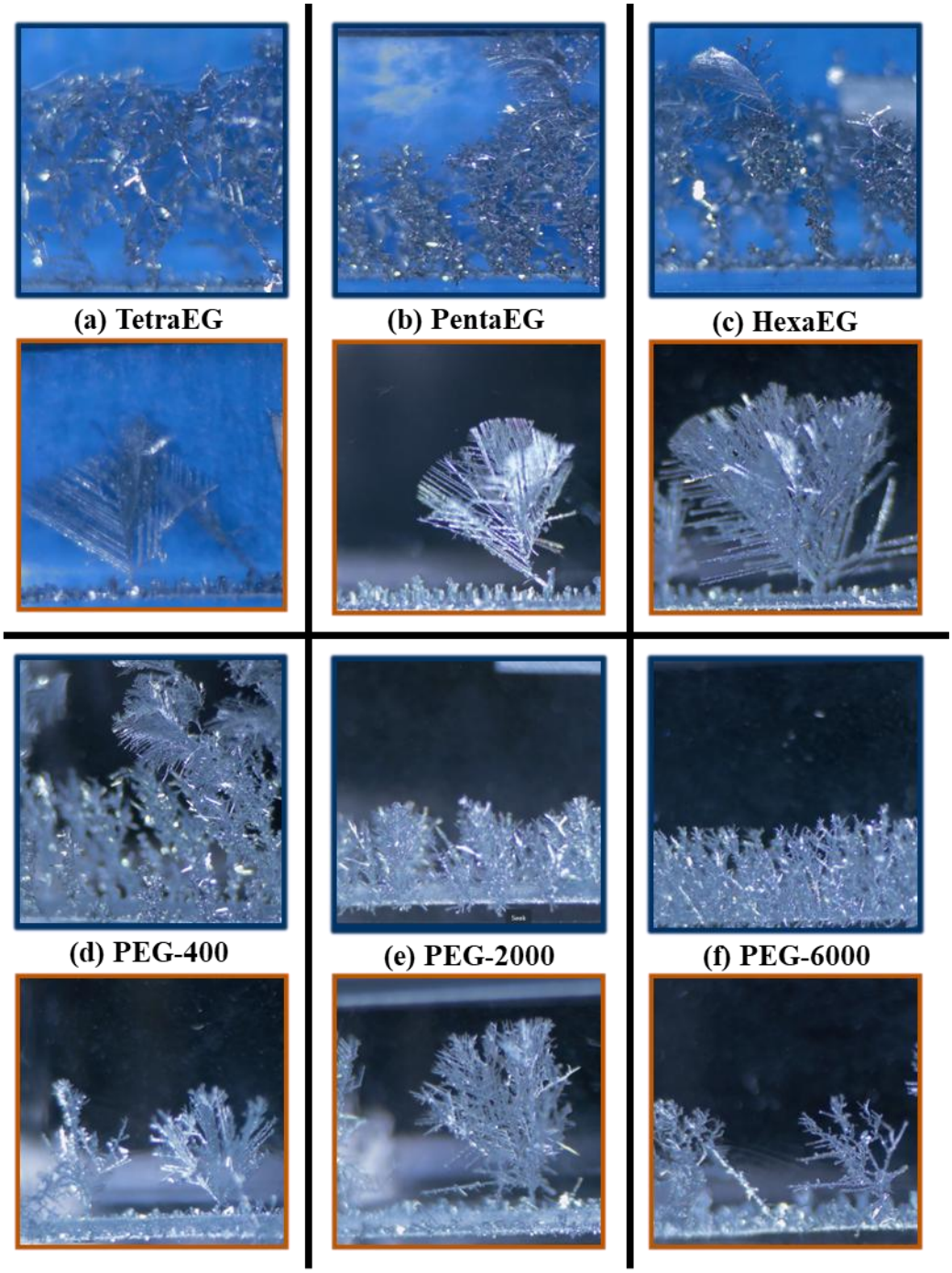

Figure S3: Enlarged optical visualization frames for tested transitions. The orange outline shows the CG mode and the blue outline shows the IN mode for each polymer additive transition shown **(a-f)** TetraEG, PentaEG, HexaEG, PEG-400, PEG-2000, PEG-6000 respectively. The transition occurred at different concentration thresholds (C_t) as shown in **Fig. 1g**.

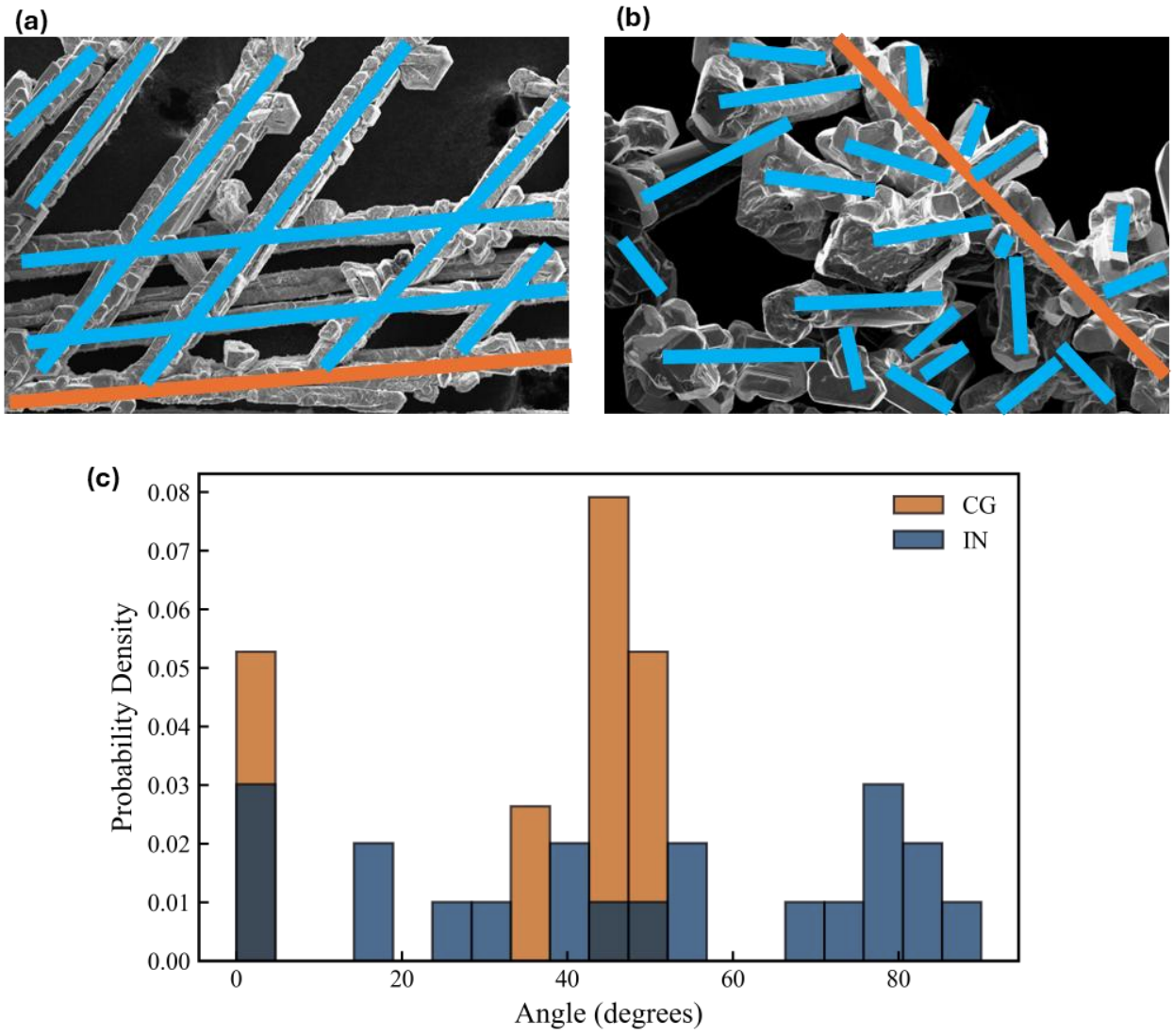

Figure S4: Distributions of dendrite branching angles from the dominant growth direction. **(a)** Annotated SEM images of dendrites formed via continuous growth (CG) mode. **(b)** Annotated SEM images of dendrites formed via independent nucleation growth (IN) mode. The blue lines were considered 'branches' and the orange line considered the reference 'backbone' of the dendrites. **(c)** Resulting probability distribution of the angles of the 'branches' relative to the 'backbone'.

The ‘branch’ angle probability distribution for CG is bimodal with 2 dominant angles of 0^{o} and 44.5^{o} (owing to the slight angle of the dendrite pictured). This indicates high levels of directional symmetry and indicates single crystalline continuous growth. In contrast, the larger spread in broader distribution of IN indicates poor symmetry and thus shows independent nucleation type growth of crystals. This provides a more quantitative evaluation for the CG vs IN growth modes.

Video S1, S2: Operando Visualization measurement samples. The videos show a 15x sped up time lapse of the experiment as described in **Fig. S1.** (s1) 1wt% ethylene glycol (EG) in 10M $ZnCl_2$ showing continuous growth mode (CG) (s2) 0.001wt% polyethylene glycol - 400 (PEG) in 10M $ZnCl_2$ showing independent growth mode (IN) at the threshold concentration. The videos show lack of HER induced bubbling regardless of CG (s1) or IN (s2) growth.

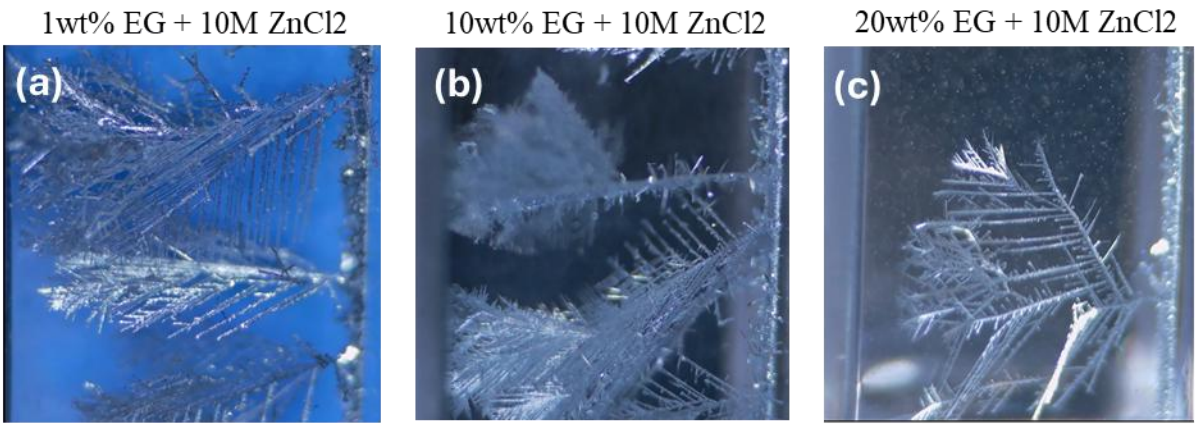

Figure S5: **Operando visualization of increasing concentration of Ethylene glycol in 10M $ZnCl_2$.** Going higher in weight percent did not change the morphology from Mode I to Mode II, implying the requirement for a minimum chain length. Going to higher concentrations made the electrolyte increasingly viscous and a poor system for electrodeposition. Furthermore, going to longer chain polymers led to lower solubility and higher viscosity, limiting the possibility of testing under the same experimental framework.

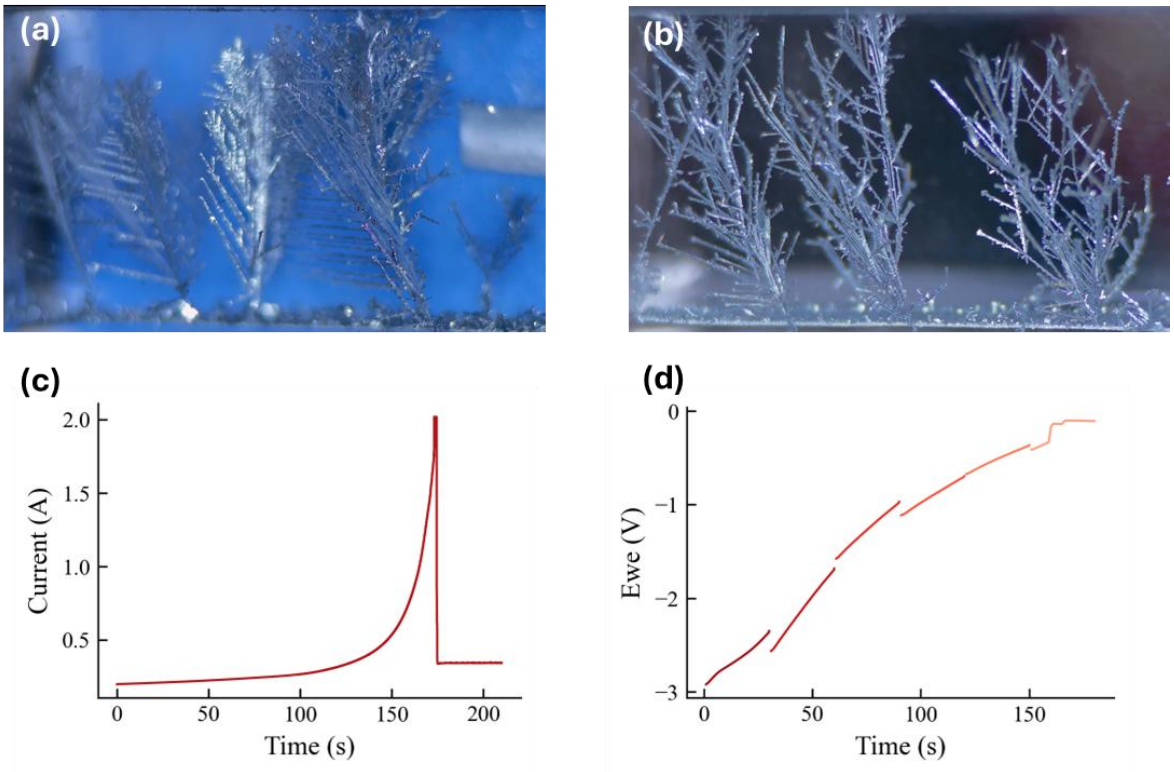

Figure S6: Comparison of Chronoamperometry (CA) and Chronopotentiometry (CP) for the same setup with 1wt% Ethylene Glycol in 10 M $ZnCl_2$. (a) Operando visualization of dendrite morphology after CA at $V_{over\text{-}limiting}$. **(b)** Operando visualization of dendrite morphology after CP at $J_{over\text{-}limiting}$. **(c)** Current Transient after CA. **(d)** Potential transient after CP.

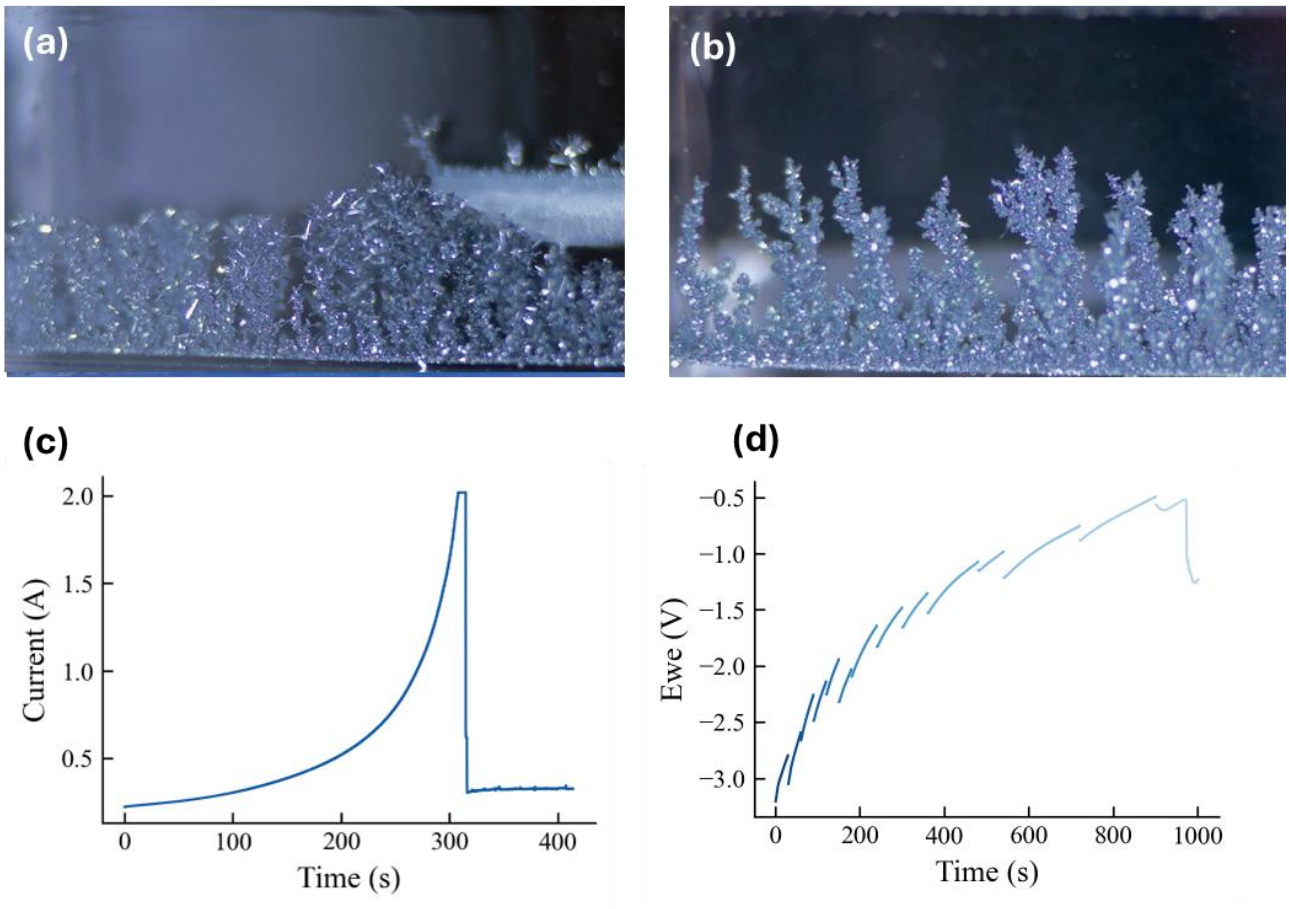

Figure S7: **Comparison of Chronoamperometry (CA) and Chronopotentiometry (CP) for the same setup with 1wt% PEG-400 in 10 M $ZnCl_2$. (a)** In Operando visualization of dendrite morphology after CA at $V_{over\text{-}limiting}$. **(b)** In Operando visualization of dendrite morphology after CP at $J_{over\text{-}limiting}$. **(c)** Current Transient after CA. **(d)** Potential transient after CP.

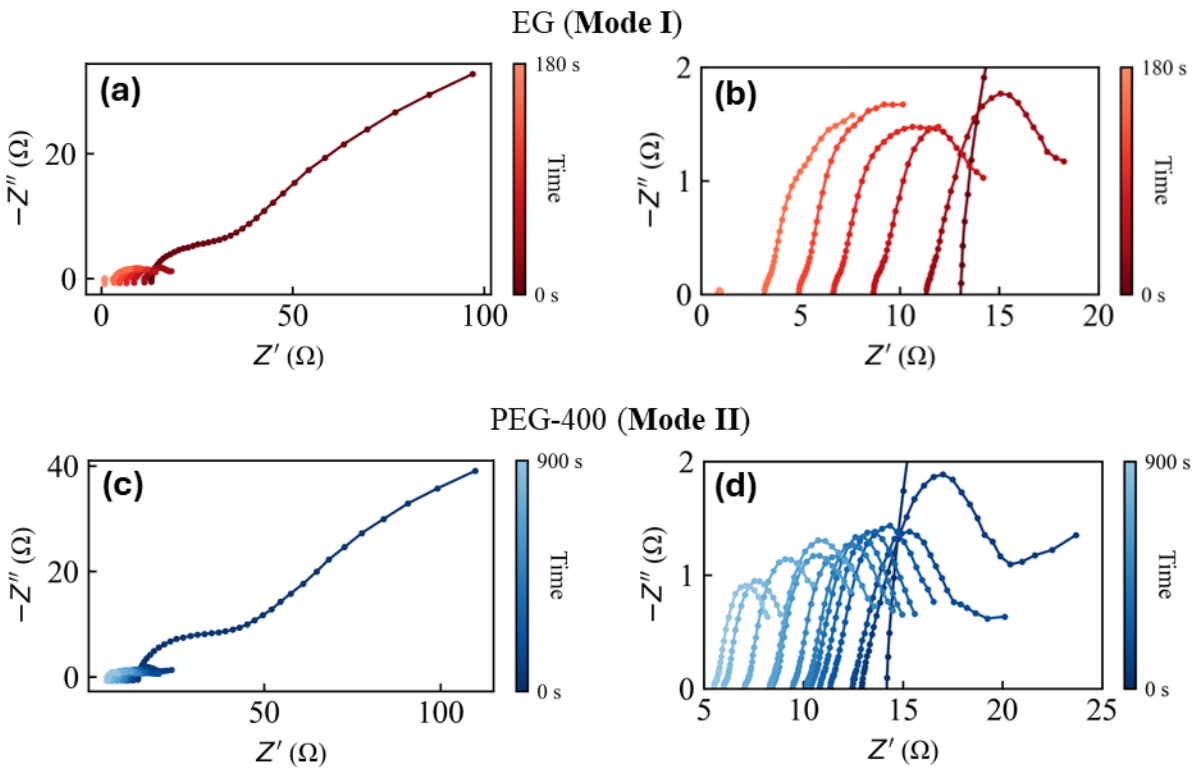

Figure S8: **Electrochemical Impedance Spectroscopy (EIS) complete results for figure 3. (a)** Complete Nyquist plot collection at all time intervals for the 1 wt.% EG system. The largest impedance curve is from the initial cell configuration. The large drop in impedance may be attributed to the loss of the oxide layer on the Zn foil electrode after initial current application and nucleation during electrodeposition. **(b)** Closer look at the impedance, with visible 0 impedance at shorting. The x intercept of these figures was used in figure 3a. **(c)** Complete Nyquist plot collection at all time intervals for the 1 wt.% PEG-400 system. **(d)** Closer look at the impedance. More time intervals had to be collected. Initially data was collected every 30s (till 180s) for both systems, but seeing as the drop in impedance for the PEG-400 was much slower, data was collected every minute and then at 3-minute intervals.

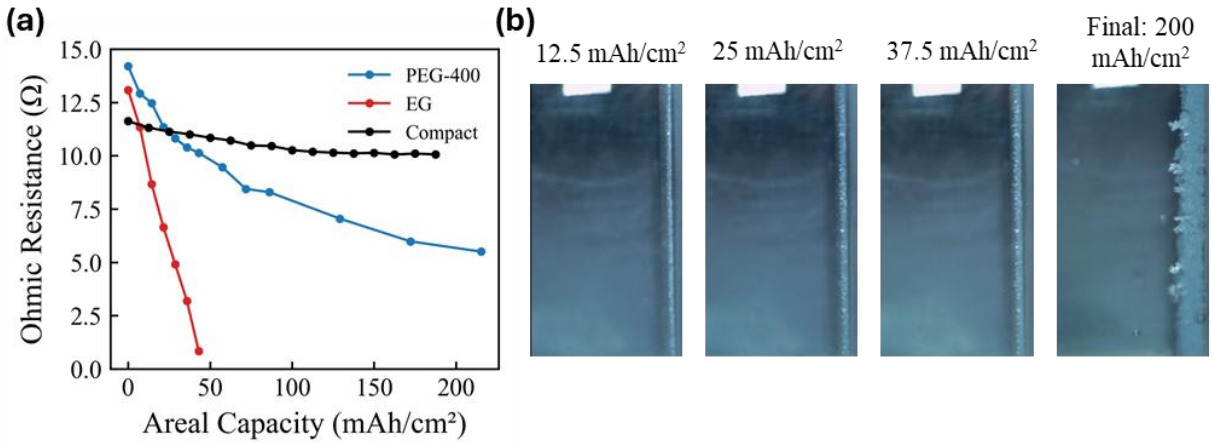

Figure S9 - Control experiment for Electrochemical Impedance Spectroscopy (EIS) and Operando optical monitoring of dendrite growth morphology. (a) Ohmic resistance R_Ω measured using EIS during constant current plating with low current density plated *compact* dendrite growth with 10M $ZnCl_2$ electrolyte. Additionally, 1 wt.% EG additive as representative for CG growth and 1 wt.% PEG-400 additive as representative for IN growth. The compact growth was conducted using the same cell set-up with a constant current electrodeposition at a current density of 4 mA/cm^2 for 200 mAh/cm^2. EIS measurements were conducted every 30 minutes. **(b)** In-operando visualization of dendrite evolution at selected time intervals for compact growth.

As shown in Fig. S9 (a), the resulting progression of RΩ shows only a minor change, consistent with minimal progression of dendrite growth front as shown in Fig. S9 (b), keeping all other conditions consistent. Comparing with the sharp changes in the EG and PEG-400 profiles with progression of dendritic growth front, the results further support that RΩ is an indicator of geometric shortening of inter-electrode distance. Hence a decrease in R_Ω indicates shortening of interelectrode distance via dendritic growth progression as corroborated by operando visualization.

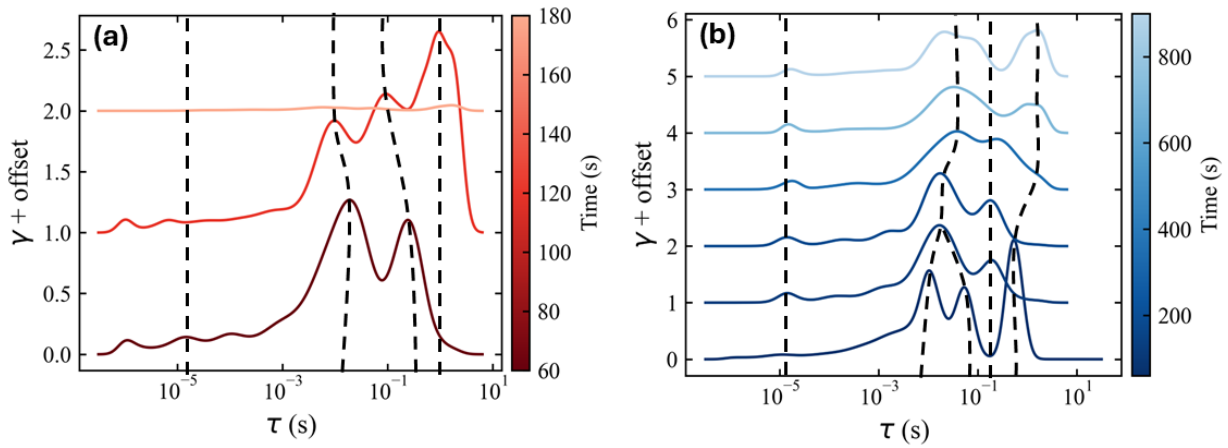

Figure S10: **Distribution of Relaxation times (DRT) for selected EIS collected in figure S8.** The change in peak heights relative to each other provides an indication for the changing source of non-ohmic impedances such as charge transfer polarization, diffusion polarization, contact polarization etc. These plots may be used in further studies to monitor the impacts of dendrite morphology and specific interfacial interactions from changing electrolytes of the system. **(a)** DRT of selected time intervals for 1wt% EG system. **(b)** DRT of selected time intervals for 1wt% PEG system.

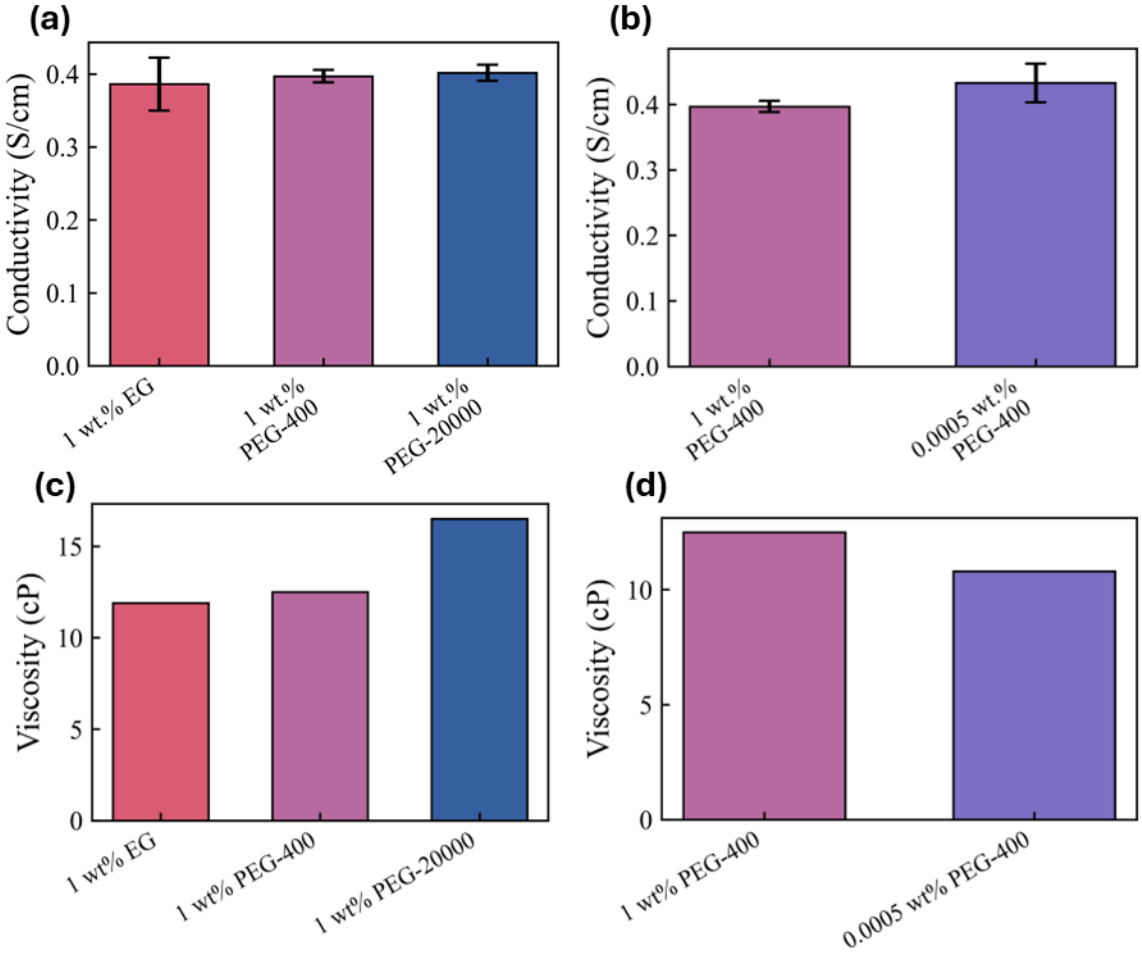

Figure S11: Bulk electrolyte properties of representative electrolytes tested. (a-b) Conductivity of the electrolyte. Calculated from EIS measured ohmic resistance of cells constructed with the electrolytes. The error bars represent the standard deviation of the replicate measurements. The conductivity values fall within a narrow range (0.386–0.433 S/cm) and do not correlate strongly with either polymer chain length or polymer concentration. **(c-d)** Viscosity of electrolytes measured using an SV-100 Viscometer. Viscosity increases with PEG molecular weight but does not correlate with the CG→IN transition, as higher-viscosity PEG-20000 does not produce a stronger IN response than PEG-400. Likewise, mild viscosity changes with PEG-

400 concentration do not explain the CG→IN boundary, indicating viscosity is not the controlling factor.

Table S1 – Calculated average conductivity values of representative electrolytes.

Electrolyte	**Average Conductivity (S/cm)**	**Standard Deviation**
1 wt% EG + 10M $ZnCL_2$	0.386	0.036
1 wt% PEG-400 + 10M $ZnCL_2$	0.397	0.009
0.0005 wt% PEG-400 + 10M $ZnCL_2$	0.433	0.029
1 wt% PEG-20000 + 10M $ZnCL_2$	0.402	0.011

Table S2 – Measured viscosity values of representative electrolytes.

Electrolyte	**Viscosity (cP)**
1 wt% EG + 10M $ZnCL_2$	11.9
1 wt% PEG-400 + 10M $ZnCL_2$	12.5
0.0005 wt% PEG-400 + 10M $ZnCL_2$	10.8
1 wt% PEG-20000 + 10M $ZnCL_2$	16.5

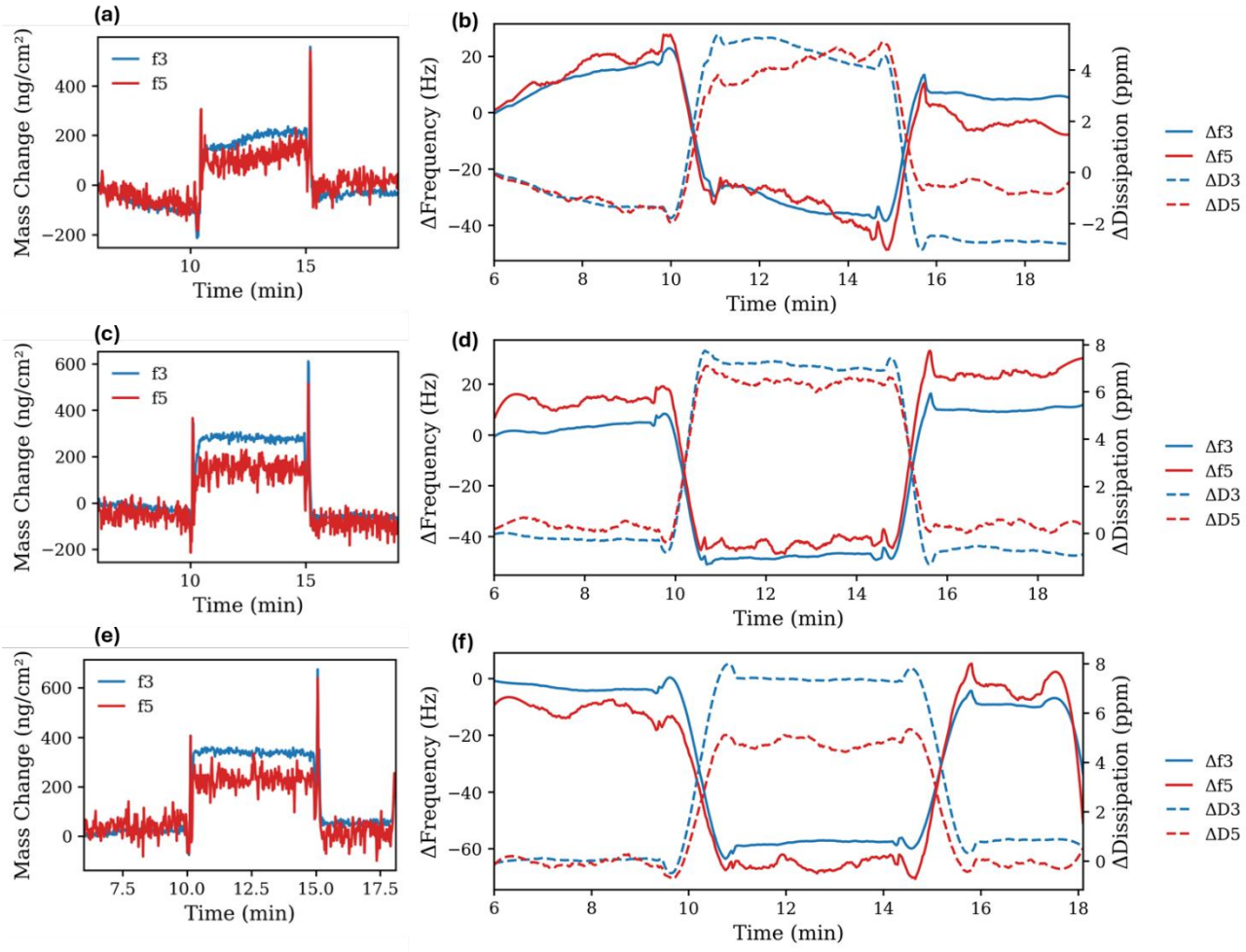

Figure S12: **QCM-D frequency and dissipation data (right) and mass change (left) for replicates for 1 wt.% EG flow system.** The Sauerbrey equation was used to calculate the mass change. Plots b, d, and f show smoothened frequency and dissipation data. However, the mass change in plots a, c, and e show the mass change calculated from the raw unsmoothed data. Average of the mass change in these plots was reported in figure 3b.

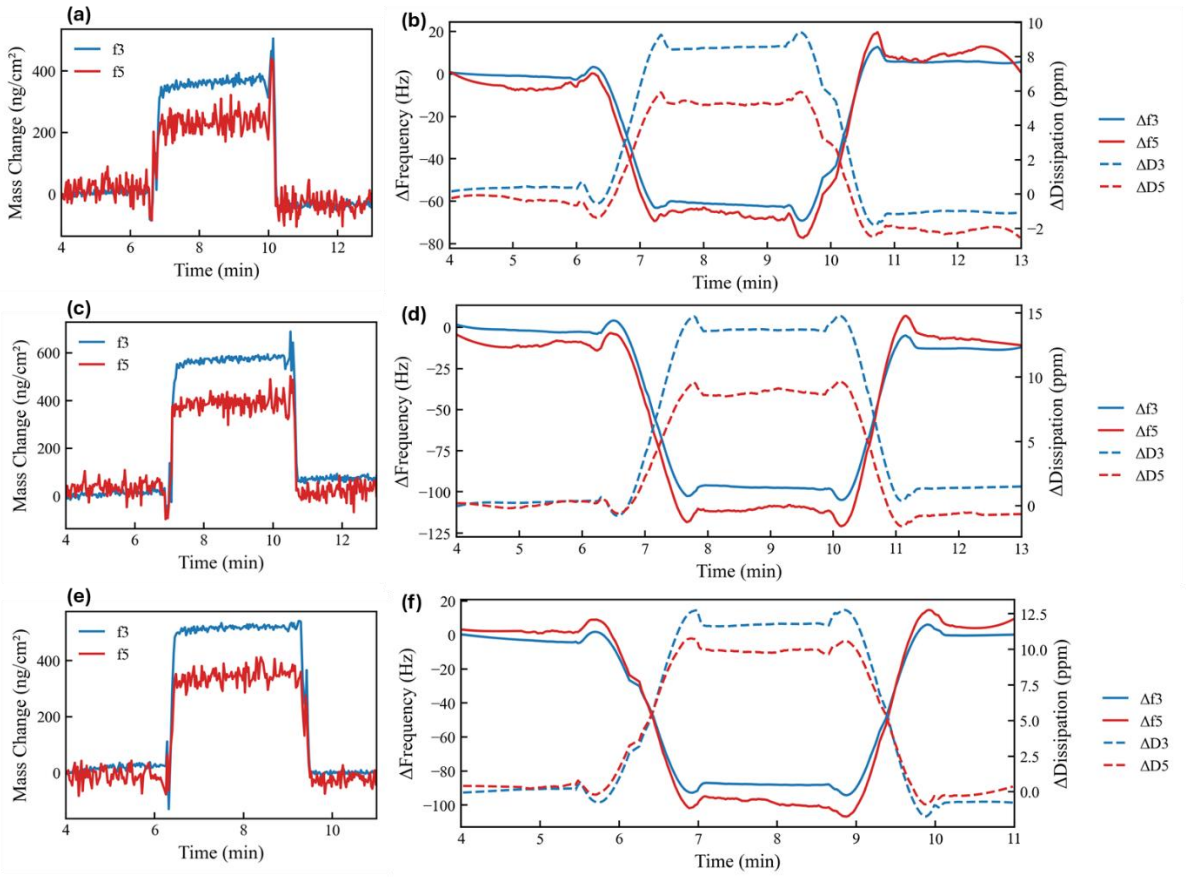

Figure S13: QCM-D frequency and dissipation data (right) and mass change (left) for replicates for 1 wt.% Tetra-EG flow system. The Sauerbrey equation was used to calculate the mass change. Plots b, d, and f show smoothened frequency and dissipation data. However, the mass change in plots a, c, and e show the mass change calculated from the raw unsmoothed data. Average of the mass change in these plots was reported in figure 3b.

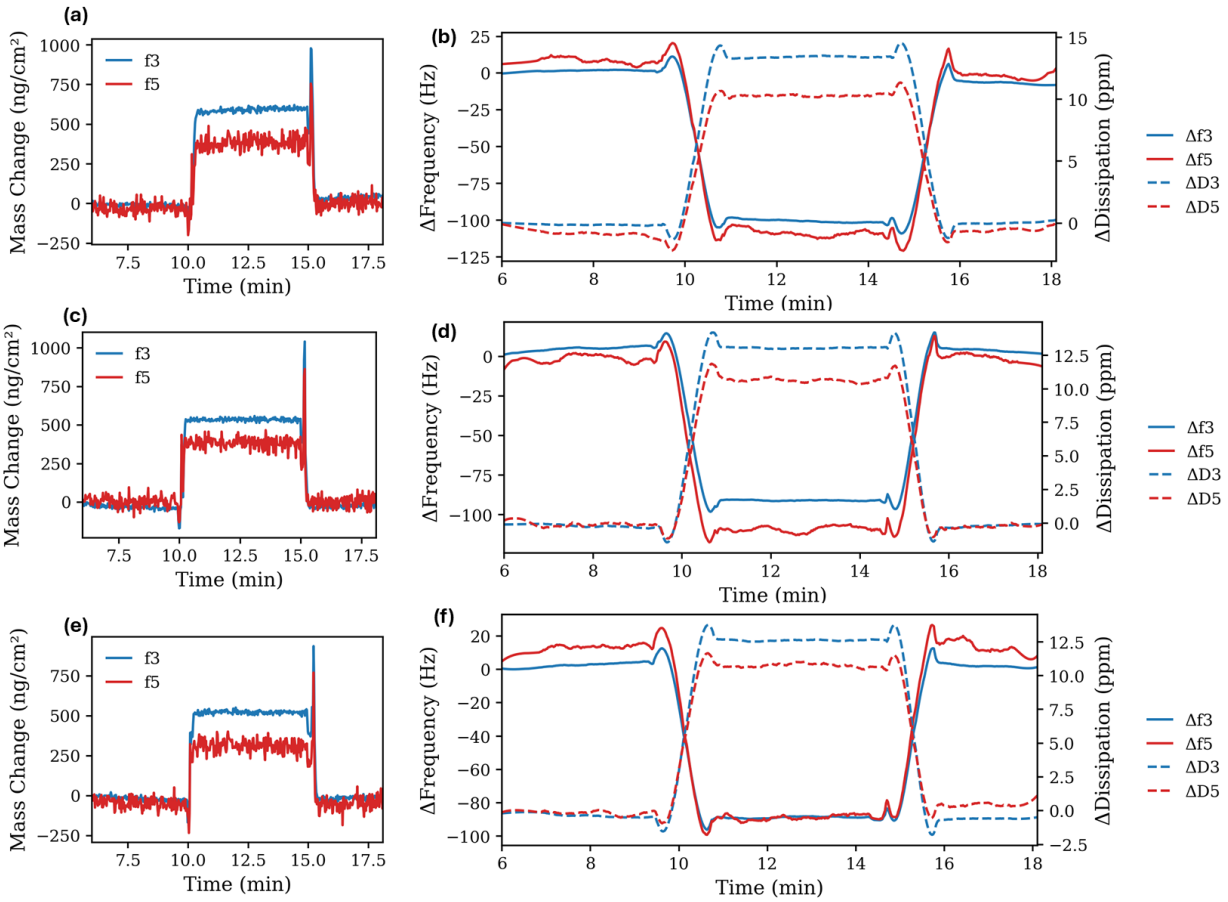

Figure S14: QCM-D frequency and dissipation data (right) and mass change (left) for replicates for 1 wt.% PEG-400 flow system. The Sauerbrey equation was used to calculate the mass change. Plots b, d, and f show smoothened frequency and dissipation data. However, the mass change in plots a, c, and e show the mass change calculated from the raw unsmoothed data. Average of the mass change in these plots was reported in figure 3b.

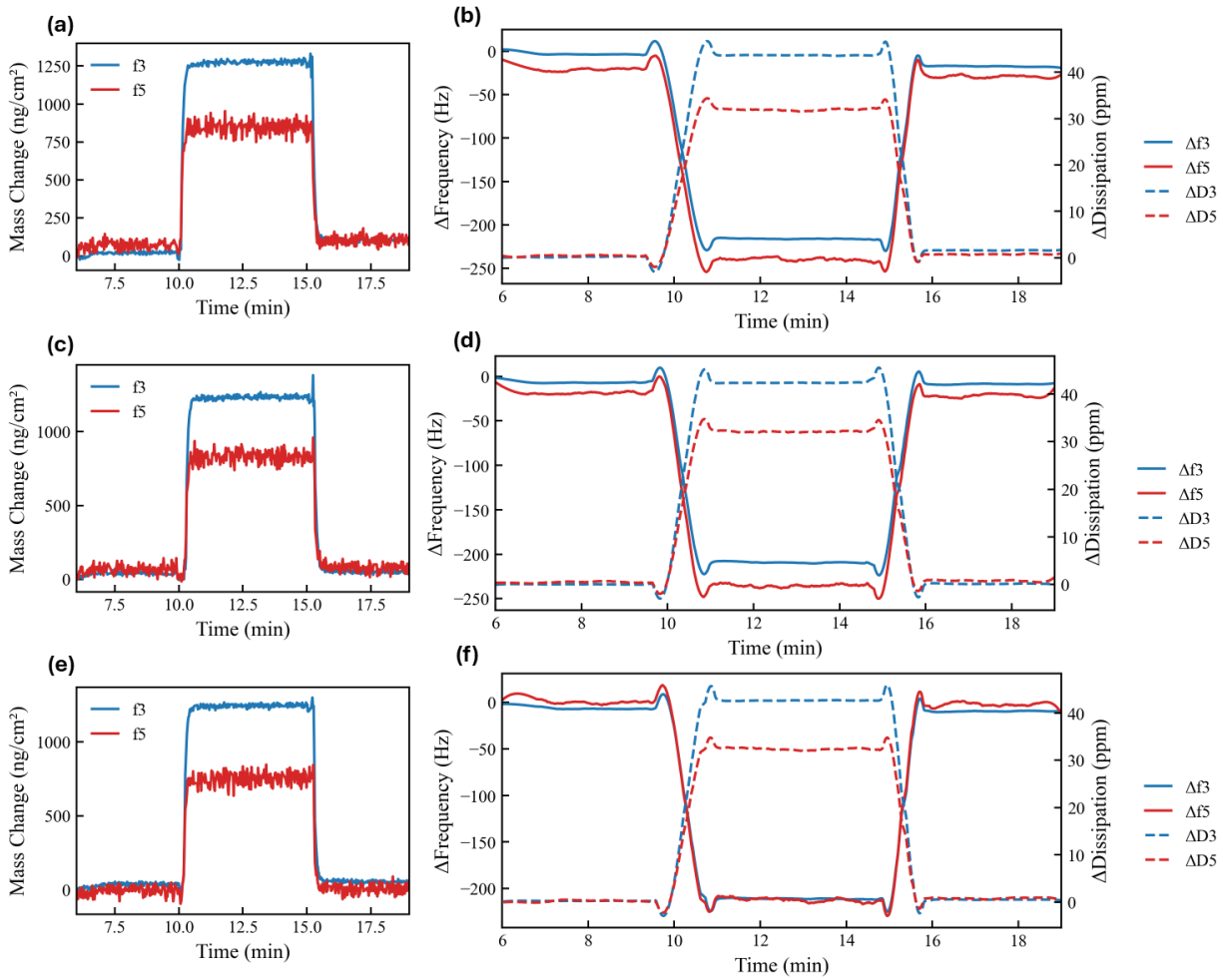

Figure S15: QCM-D frequency and dissipation data (right) and mass change (left) for replicates for 1 wt.% PEG2000 flow system. The Sauerbrey equation was used to calculate the mass change. Plots b, d, and f show smoothened frequency and dissipation data. However, the mass change in plots a, c, and e show the mass change calculated from the raw unsmoothed data. Average of the mass change in these plots was reported in figure 3b.

Note S1: Analyzing the QCM-D measurements. An electrochemically compatible gold sensor was used, and the electrolyte flowed at a constant flow rate over the sensor. Four representative electrolytes were flowed over the sensor, and the frequency change was monitored – 1 wt.% of Ethylene glycol, Tetra ethylene glycol, PEG-400, and PEG-2000. The Sauerbrey equation was used to extract mass change information from the raw data. The Saurbrey equation is provided as follows:

$$\Delta m = -C \frac{\Delta f}{n} \qquad \text{Equation (4)}$$

where Δm is mass change, Δf is the change in resonance frequency, C is the mass sensitivity constant, and n is the harmonic number (odd integers).[12]

The 3rd and 5th resonance frequencies were used to calculate mass change using this method. A representative data set is shown in **Fig. 3a, c**. The bump in mass change in panel (a) corresponds to the drop in frequency in panel (c). The Sauerbrey theory was further applied to extrapolate an approximation for the thickness of the polymer layer formed on the electrode as shown in figure S16.

It must be noted that the Sauerbrey equation applies to thin rigid films. Since we know fluid being tested is viscoelastic (as discussed in the main text), these values are purely an underestimated approximation and should be studied for comparative purposes rather than absolute values. Further accuracy may be achieved by using better models to fit the QCM-D data such as Voigt or Kelvin-Voigt viscoelastic models.[12]

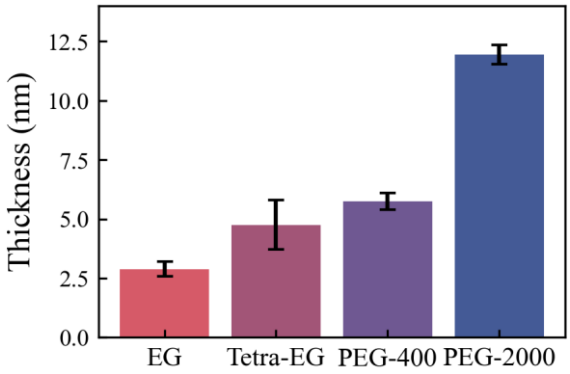

Figure S16: **Thickness of adsorbed polymer layer from QCM-D data.** The Sauerbrey theory was used to calculate average thickness from the mass change observed in **Fig. S12-S15**.

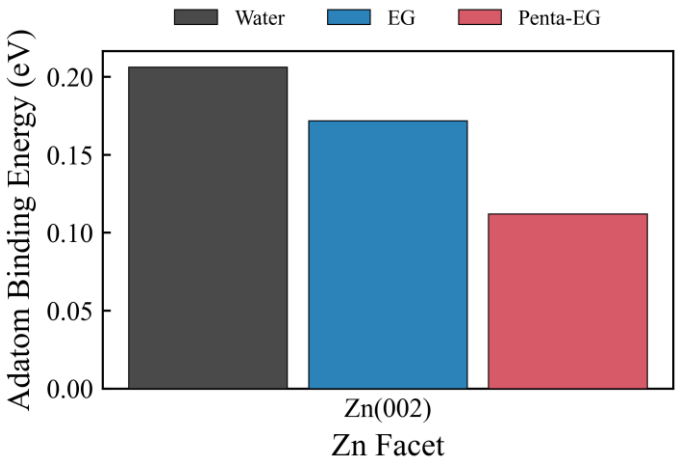

Figure S17: DFT calculations of the solvent stabilized Zn adatom binding energy on various surfaces. The large negative value comes from surface reconstructions due to the presence of solvent molecules and the adatom.

One way the solvent molecule can change the growth rate of a surface is by stabilizing the newly deposited adatoms on the surface. The adatoms usually have a positive binding energy and are unstable because they are undercoordinated compared to atoms in the bulk. The adatoms therefore are driven by thermodynamics to assimilate into the surface to achieve a more bulk-like binding environment. Both EG and PEG can stabilize the adatoms, but PEG molecules have a stronger stabilization effect.

We have studied the (002), (100), (101), (102), (103), $(21\overline{3})$ surfaces. We didn't present the adatom binding energy non-(002) surfaces because these surfaces can reconstruct when solute molecules and adatoms are introduced. The resulting geometries are highly isotropic, and comparing adatom binding energies in the presence of different solute molecules is not meaningful. The adatom binding energies obtained on the (100) surface for water, EG, and penta-EG are 0.89, 1.10, 0.61 eV, respectively. The reconstructed (100) surface resembles the (002) surface.

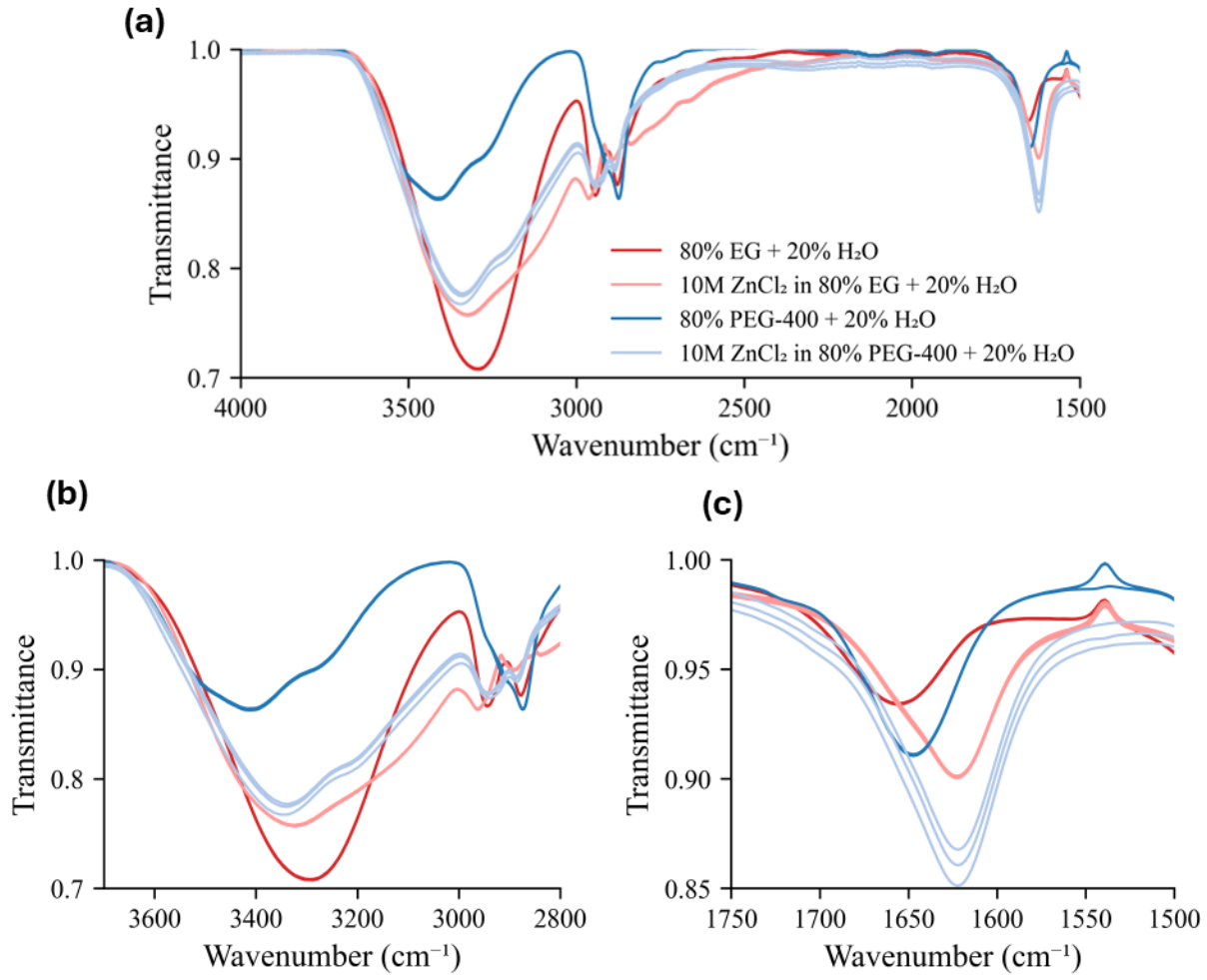

Figure S18: Fourier Transform Infrared Spectroscopy results of chosen systems for each growth mode. The solutions were chosen in this composition to ensure the spectrum was not purely dominated by the hydrogen bonding in water, to more clearly see the interaction between the polymer and hydrated salt. (a) Full spectrum. (b)-(c) Hydroxide bond vibrations. The hydroxide bending peak is focused on in panel (c) and shows a smaller red shift in the PEG-400 system in comparison to the EG system. This indicates a stronger hydrogen bonding network in the PEG-400 system; in line with the NMR results.

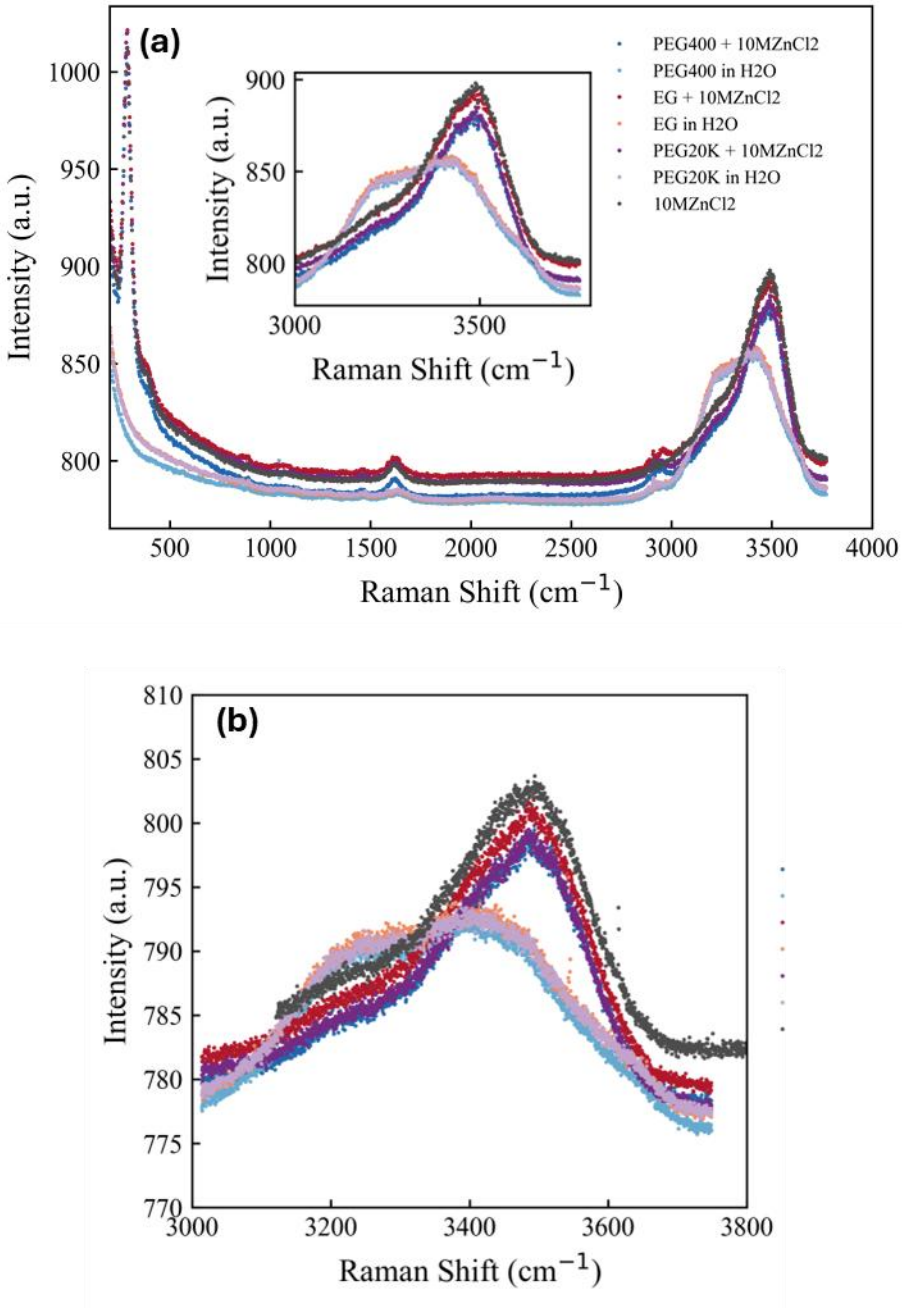

Figure S19: Raman Spectroscopy results of representative electrolytes (1 wt.% additives) for each growth mode. (a) 600 grating full spectra. The inset shows the O-H bending vibration. **(b)** 1800 grating spectra, focused on the same O-H bending vibration. The true concentrations of the electrolyte were chosen to make these measurements. Though the alignment between the systems with and without $ZnCl_2$ suggests that to be the dominating effect.

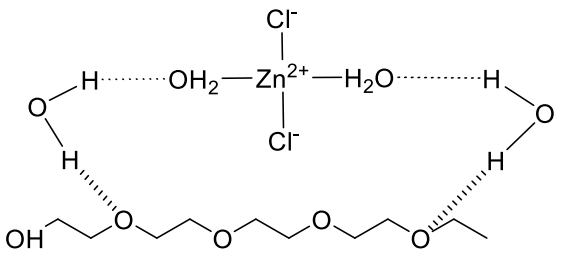

Figure S20: Proposed molecular interaction scheme for longer chain PEG molecules. This molecular structure provides an explanation for the rightward shift observed by the addition of the salt during NMR experiments.[13]

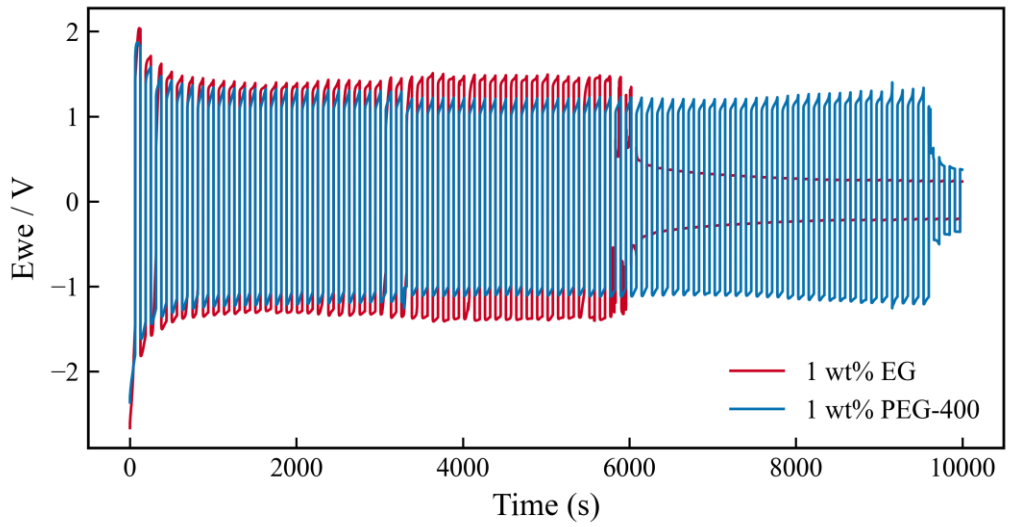

Figure S21: Cycling performance of both growth modes. The voltammograms of representative systems for each growth mode. Conditions for plating-stripping cycles were at constant current of 344.4 mA and capacity of 15 mAh/cm^2 with 1 wt.% EG additive as representative for CG growth and with 1 wt.% PEG-400 additive as representative for IN growth. The drop in potential in indicative of shorting in the cell, with the EG system always shorting before the PEG-400 system in trials despite the stochastic nature of the experiments.

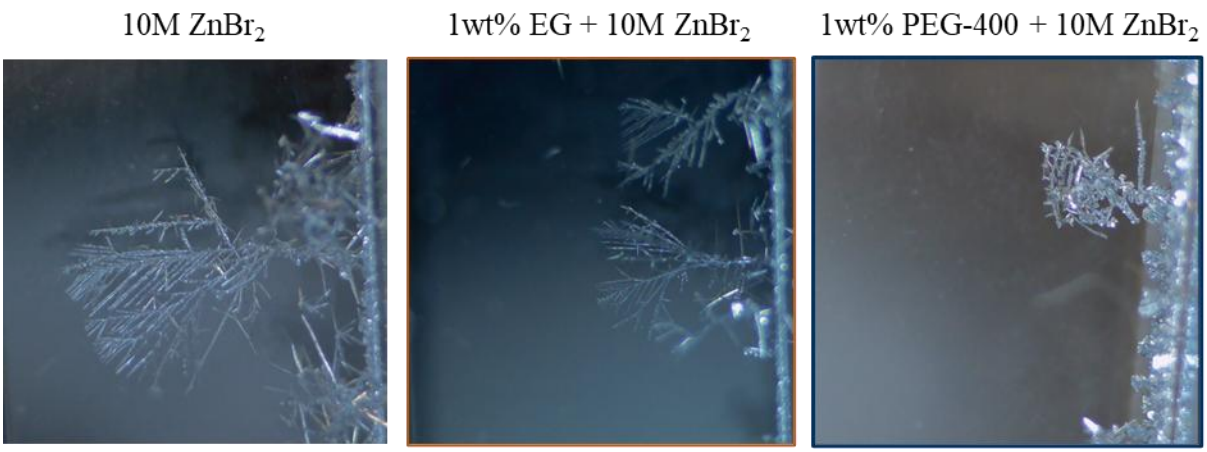

Figure S22: **Operando visualization of increasing representative systems with 10M $ZnBr_2$.** 1 wt.% EG was selected for Mode I growth, while 1 wt.% PEG-400 was used for Mode II growth. The resemblance between the 10 M $ZnBr_2$ system and the 1 wt.% EG + 10 M $ZnBr_2$ system, in contrast to the different morphology observed in the PEG-400 system, further corroborates the proposed framework under an alternative electrolyte environment.

References

(1) Zheng, J.; Archer, L. A. Controlling electrochemical growth of metallic zinc electrodes: Toward affordable rechargeable energy storage systems. *Science Advances* **2021**, *7* (2), eabe0219.
(2) Jiang, H.; Tang, L.; Fu, Y.; Wang, S.; Sandstrom, S. K.; Scida, A. M.; Li, G.; Hoang, D.; Hong, J. J.; Chiu, N.-C. Chloride electrolyte enabled practical zinc metal battery with a near-unity Coulombic efficiency. *Nature Sustainability* **2023**, *6* (7), 806-815.
(3) Jao, W.-Y.; Sheyfer, D.; Micha, J.-S.; Aggarwal, A.; Higdon, H.; Hu, C.-C.; Zheng, J. X. K. Dendritic Growth in Battery Anodes: On the Hidden Role of Crystallographic Anisotropy at Propagating Electrochemical Interfaces. **2025**.
(4) Kresse, G.; Furthmüller, J. Efficiency of ab-initio total energy calculations for metals and semiconductors using a plane-wave basis set. *Computational materials science* **1996**, *6* (1), 15-50.
(5) Kresse, G.; Furthmüller, J. Efficient iterative schemes for ab initio total-energy calculations using a plane-wave basis set. *Physical review B* **1996**, *54* (16), 11169.
(6) Kresse, G.; Hafner, J. Ab initio molecular dynamics for liquid metals. *Physical review B* **1993**, *47* (1), 558.
(7) Kresse, G.; Joubert, D. From ultrasoft pseudopotentials to the projector augmented-wave method. *Physical review b* **1999**, *59* (3), 1758.
(8) Blöchl, P. E. Projector augmented-wave method. *Physical review B* **1994**, *50* (24), 17953.
(9) Perdew, J. P.; Burke, K.; Ernzerhof, M. Generalized gradient approximation made simple. *Physical review letters* **1996**, *77* (18), 3865.
(10) Grimme, S. Semiempirical GGA-type density functional constructed with a long-range dispersion correction. *Journal of computational chemistry* **2006**, *27* (15), 1787-1799.
(11) Monkhorst, H. J.; Pack, J. D. Special points for Brillouin-zone integrations. *Physical review B* **1976**, *13* (12), 5188.
(12) Johannsmann, D.; Langhoff, A.; Leppin, C. Studying soft interfaces with shear waves: Principles and applications of the quartz crystal microbalance (QCM). *Sensors* **2021**, *21* (10), 3490.
(13) Jin, S.; Yin, J.; Gao, X.; Sharma, A.; Chen, P.; Hong, S.; Zhao, Q.; Zheng, J.; Deng, Y.; Joo, Y. L. Production of fast-charge Zn-based aqueous batteries via interfacial adsorption of ion-oligomer complexes. *Nature communications* **2022**, *13* (1), 2283.